Frontiers in Heat and Mass Transfer (FHMT), 19, 33 (2022)
DOI: 10.5098/hmt.19.33

Global Digital Central
ISSN: 2151-8629

Frontiers in Heat and Mass Transfer

Available at www.ThermalFluidsCentral.org

VAPOUR ABSORPTION PROCESS IN AN $NH_3/LINO_3$ BUBBLE ABSORBER USING AN OPTIMIZED CFD MODEL

Andrés Zapata[a], Carlos Amaris[b*], Alexis Sagastume[a], Andrés Rodríguez[a]

Energy Department, Universidad de la Costa, Barranquilla, Atlántico, 080002, Colombia
School of Mechanical Engineering, Universidad Industrial de Santander, Bucaramanga, Santander, 680002, Colombia

ABSTRACT

The present study aims to assess the vapour bubble absorption into the ammonia/lithium nitrate ($NH_3/LiNO_3$) solution by using an optimized CFD model. A detailed methodology to build up the CFD model is presented, as well as its validation using experimental data. The operating conditions set corresponds to an absorption chiller driven by low-temperature heat sources such as solar energy in warm environments. Results evidenced that the Volume of Fluid and Mixture models are adequate to be used in the CFD model to predict the absorption process in the bubble absorber assessed depending on the mesh density refinement. Moreover, the heat transfer coefficient from the solution side and the absorption mass flux are the variables needed for reliable validation of the model. Finally, the absorbed flux estimated from the CFD model ranged between 3.2×10^{-3} kg.m^{-2}.s^{-1} and 4.4×10^{-3} kg.m^{-2}.s^{-1}, while the solution side heat transfer coefficient varied between 457 W.m^{-2}.K^{-1} and 786 W.m^{-2}.K^{-1}, under the conditions considered.

Keywords: CFD model, absorption chiller, ammonia, lithium nitrate, bubble absorber.

1. INTRODUCTION

Absorption chillers are identified as sustainable and environmentally friendly cooling technologies when activated by renewable energy sources (Florides et al., 2002; Ullah et al., 2013; Mendoza et al., 2021; Rodríguez-Toscano et al., 2022; Amaris et al., 2023) or by waste heat (Ayou et al., 2013; Amaris et al., 2020b). The basic configuration of absorption cooling systems (VARs) consists of an evaporator, a condenser, an expansion device, a solution heat exchanger, a solution pump, an absorber, and a generator. Because of the simultaneous transport phenomena occurring in absorbers and generators, these are considered the most critical components of VARs (Amaris et al., 2018, 2020a; Amaris and Bourouis, 2021). The development of these transport phenomena directly affects the global performance of absorption refrigeration systems. Therefore, understanding the development of the heat and mass transfer processes is essential to improving the overall performance of VARs. Particularly, there are diverse designs of absorbers, including falling film absorbers, adiabatic absorbers, and bubble absorbers. Specifically, bubble absorbers have been proved to provide larger heat and mass transfer rates contrasted to falling film units (Kang et al., 2000; Wu et al., 2018).

There are different working fluids used in VARS, although the ammonia/water (NH_3/H_2O) and water/Lithium Bromide (H_2O/LiBr) are the most widely used. However, the $NH_3/LiNO_3$ mixture provides some advantages like lower heat source temperatures contrasted to those of NH_3/H_2O chillers, and no risk of crystallization in warm climates as compared to the use of H_2O/LiBr chillers (Aggarwal and Agarwal, 1986; Oronel et al., 2010; Amaris et al., 2015). Therefore, assessing the performance of absorbers with $NH_3/LiNO_3$ chillers is required to further contribute to its development and diffusion. To this end, experimental research is fundamental to testing and designing the different components of VARS. However, experimental studies are usually costly, so alternative research paths can be followed to overcome this economic barrier. Numerical and analytical studies allow for a deep understanding of the heat and mass transfer phenomena at the interface of multiphase flows (Merrill and Perez-Blanco, 1997; Elperin and Fominykh, 2003; Suresh and Mani, 2010; Triché et al., 2017; Turkyilmazoglu, 2019, 2021; Zhou et al., 2023). These studies involved the modelling of the effect of nanofluids on an ammonia falling film (Zhou et al., 2023), numerical evaluation a moving bed heat exchanger (Turkyilmazoglu, 2019), analytical assessment of falling film absorber with constant mass fraction, (Turkyilmazoglu, 2021), and the phenomenological theory analysis of a bubble absorber (Suresh and Mani, 2010). Additionally, computational fluid dynamics (CFD) is an adequate alternative to experimental investigation. The use of CFD facilitates assessing and optimizing the performance of thermal processes and equipment at a lower cost and difficulty, provided a reliable validation of the model. Therefore, the identification of adequate simulation conditions and multiphase models to simulate different flow patterns and complex heat and mass transfer processes is of interest in sustainable energy conversion systems (Karima et al., 2018; Anand et al., 2020; Mirzaie et al., 2020; Soheel et al., 2021; Bhagat and Deshmukh, 2022).

Given the complexity of modelling heat and mass transfer processes in absorbers or generators used in VARs, the open literature discussing the use of CFD to model these components is limited. The CFD modelling was used to assess a membrane-based absorber using H_2O/LiBr (Asfand et al., 2015), also H_2O/(LiBr + LiI + $LiNO_3$ + LiCl) and H_2O/($LiNO_3$ + KNO_3 + $NaNO_3$) (Asfand et al., 2016), a falling film absorber using H_2O/LiBr (Hosseinnia et al., 2016, 2017), a bubble absorber using R134a-DMF (Panda and Mani, 2016), a plate bubble absorber using NH_3/H_2O (Lima et al., 2019), and a first approach of the absorption using $NH_3/LiNO_3$ (Zapata et al., 2021). Moreover, Asfand et al. (2015) reported a CFD model to analyse the local heat and mass transfer mechanisms in an H_2O/LiBr membrane-based absorber. In this CFD model, the laminar model and model Mixture were linked to

* *Corresponding author. Email: Cfamacas@uis.edu.co*

Global Digital Central
ISSN: 2151-8629

simulate the phases contact. The authors showed that the solution film thickness is a key indicator affecting vapour absorption. In this case, the model was validated by comparing the predicted data series with experimental results, showing a mean absolute error of 4.82% with a standard deviation of 0.0322.

Panda et al. (2016) developed a CFD model to evaluate the effect of two 4.8 mm inner diameter injectors on the absorption process in a bubble absorber using R134a-DMF. The model used the k-ω SST turbulent model linked to the Mixture model to simulate the phase contact. Results show that contrasted to a vertical nozzle with no swirl, the mass transfer coefficient increased between 120% and 170%, while the heat transfer coefficient increased from 20% to 40% in swirl flow.

Hosseinnia et al. (2016, 2017) modelled the drop and jet flows of a falling film of H_2O/LiBr on tubes. The phases interface was modelled with the volume of fluid model (VOF). The CFD model was validated using the Nusselt's solution, reporting an error around 0.01%. Moreover, results demonstrated that the absorption mass flux rate decreases when the flow regime changes from drops to jets.

Lima et al. (2019) developed a CFD model to assess a flat plate bubble absorber using NH_3/H_2O. The model considers the k-ε turbulent model, and the Navier Stokes approach to simulate the heat and mass transfer processes. The CFD model was validated with experimental data reported by Kang et al. (1998) for an offset strip fins plate absorber, and Cerezo (2006) for a corrugated plate absorber. The results showed errors of 8.2%, 4.2%, and 18.5%, for the cooling water temperature, solution flow temperature, and outlet NH_3 concentration, respectively, at the absorber outlet. Finally, Zapata et al. (2021) simulated the performance of an $NH_3/LiNO_3$ bubble absorber using a CFD model, reporting error values lower than 10% for the mass transfer and 7% for the heat transfer coefficient of the solution.

While the studies available in the specialized literature evidenced the potential of the CFD modelling to assess the different absorber configurations, there are methodological aspects that need to be discussed in more detail. Specifically, there is no consistent and detailed methodology to select the multiphase model, develop the mesh independence test, and validate the model. In that sense, the CFD models to simulate absorbers discussed in the scientific literature lack a detailed methodology and a reliable validation of the model results. CFD models are validated using experimental data. Therefore, the reliability of those CFD models to accurately calculate heat and mass transfer variables for the different values of operating parameters like the flow and temperature of the solution and cooling flows is not demonstrated.

This study presents the assessment of the heat and mass transport in an $NH_3/LiNO_3$ tubular bubble absorber by developing an optimized CFD model. The study discusses the absorber performance for different mesh refinements, and multiphase models, and presents an appropriate methodology for model validation. Therefore, the present study focuses on the absorber performance considering global heat and mass transfer parameters. This research aims to contribute to the development of CFD models to assess and design absorbers for VARs.

2. METHODOLOGY

2.1 Test section and operating conditions

The absorber considered in this study is a double pipe heat exchanger (see Fig. 1). The refrigerant injector located at the bottom of the inner tube has a thickness of 0.002 m. Table 1 shows the geometric characteristics of the absorber.

In this configuration, both the solution mass and refrigerant vapour mass flowed up in the inner tube. Moreover, the cooling water flowed downward through the annular side.

The conditions set for the CFD simulation are presented in Table 2 for an ammonia mass composition set at 45.0%. Those conditions are of interest for $NH_3/LiNO_3$ absorption chillers activated with low-temperature heat sources in high heat dissipation environments (Amaris, 2013).

The CFD absorber model performance was assessed by comparing the model results for the temperature of the solution and ammonia mass fraction at the absorber outlet, the absorbed mass flux, and the solution side heat transfer coefficient to experimental data. The absorbed mass flux was determined considering the solution flow and ammonia concentration at the absorber inlet and outlet and in the internal tube surfaces area. The absorber outlet solution temperature and ammonia mass fraction as well as the solution side heat transfer coefficient were obtained directly from the simulation.

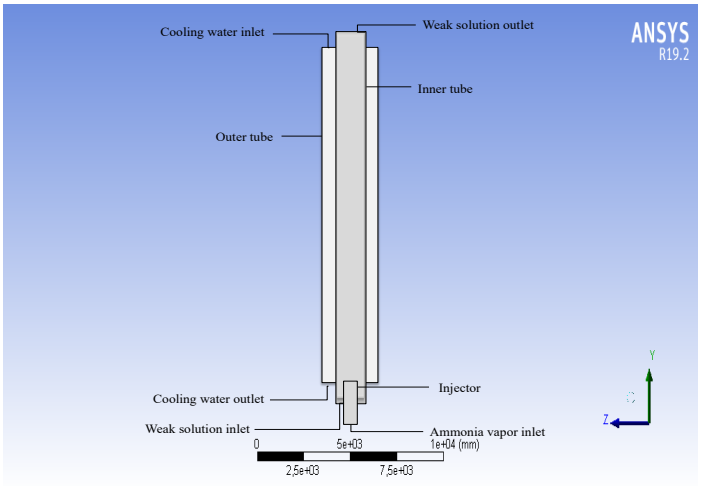

Fig. 1 Bubble absorber model.

Table 1 Geometric dimensions of the absorber.

Component	*Outer tube* (mm)	*Inner tube* (mm)	*Injector* (mm)
External diameter	15	9.5	3.7
Hydraulic diameter	3.5	7.5	1.7
Length	1000	1100	8.0

Table 2 Simulation conditions for the CFD model.

Fluid	*Mass Flow* ($kg.h^{-1}$)	*Temperature* (K)	*Pressure* (Pa)
Water	91.1 – 110	308 – 314	2.0×10^5
$NH_3/LiNO_3$ mixture	20 – 72	319	5.2 x 105
NH_3 vapour	0.01	298.15	5.5×10^5

2.2 CFD model development

Geometry and mesh design, the ANSYS Fluent® (V.19.2) interface was used to develop the 3D-CFD model, using a Dell Precision TX3500 workstation with an Intel®Xeon® X3470 processor. The finite volume method was used for the discretization of the model.

The mesh quality was assessed using the orthogonal quality and skewness methods, guarantying values above 0.97 (SD 0.20) for the meshes considered. The quality of mesh elements is higher for values closer to 1.0. The mesh quality assessment procedure was performed to guarantee adequate solution accuracy and model convergence. Fig. 2 illustrates the geometry of the 3D model.

Global Digital Central
ISSN: 2151-8629

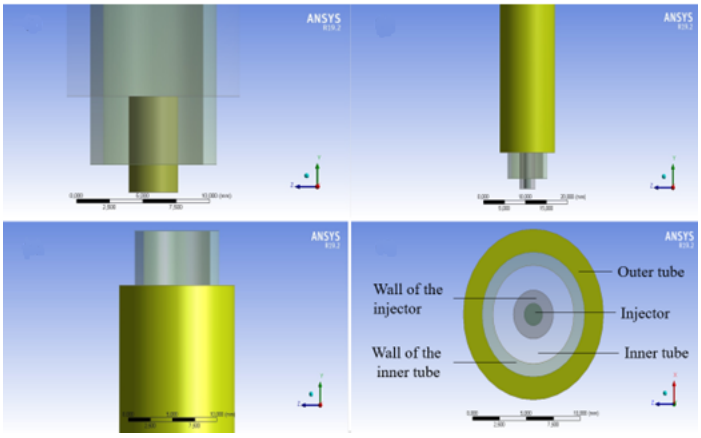

Fig. 2 3D absorber views.

Mesh study, to assess the model performance, four mesh cases with different cells were studied:

1) Elements: 27402 (generating 83576 nodes),
2) Elements: 87326 (generating 261978 nodes),
3) Elements: 128877 (generating 230791 nodes),
4) Elements: 554804 (generating 846193 nodes).

Fig. 3 depicts the meshes considered in cases 1 and 3 for the 3D model.

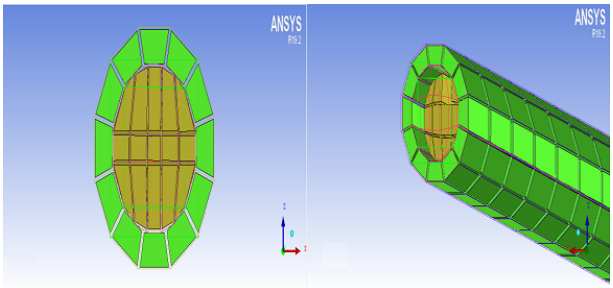

(a) Base case

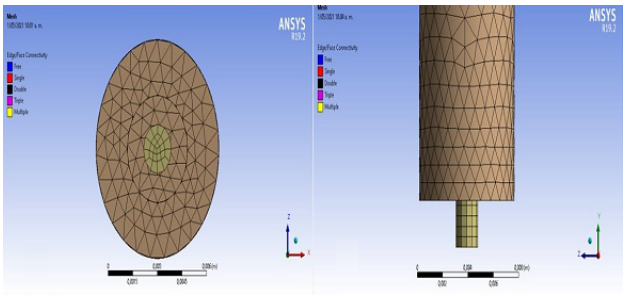

(b) Optimized model

Fig. 3 Meshes considered for the discretization of the model (a) base case and (b) optimized model.

Multiphase Models, two multiphase models were used for the purpose of the study: volume of fluid (VOF) for the base case and Mixture in the optimization. Moreover, four Eulerian Phases were considered in the model:

- Phase 01 for the NH_3/$liNO_3$ solution flow,
- Phase 02 for the NH_3 vapour flow,
- Phase 03 for the cooling water flow,
- Phase 04 for the NH_3 liquid flow,

The mass transport mechanisms were considered from phase 02 to phase 01 as well as from phase 02 to phase 04 with constant rates (1/s) equal to 0.02 and 0.14 respectively. The simulations were developed using the realizable k-epsilon viscous models. Finally, the energy equation was used to simulate the heat transfer processes.

Governing equations, these equations rely on the Navier-Stokes approach solved under transient conditions for each case. The 3D continuity, turbulence, energy, and momentum approaches are shown below (Eq. 1-5). The model and its equations were solved using a Eulerian multiphase method.

Continuity equation

$$\frac{\partial}{\partial t}(\alpha_q \delta_q) + \nabla(\alpha_q \delta_q \vec{V_q}) = \sum_{p=1}^{n}(\dot{m}_{pq} - \dot{m}_{qp}) + S_q \quad (1)$$

Equation for momentum

$$\frac{\partial}{\partial t} = (\rho\vec{v}) + \nabla.(\rho\vec{v}\vec{v}) = -\nabla_p + \nabla.(\bar{\bar{\tau}}) + \rho\vec{g} + \vec{F} \quad (2)$$

Model for Turbulence

The $k-\varepsilon$ Realizable model equations for turbulence are:

$$\frac{\partial}{\partial t}(\rho k) + \frac{\partial}{\partial x_j}(\rho k u_j) = \frac{\partial}{\partial x_j}\left[\left(\mu + \frac{\mu_t}{\sigma_k}\right)\frac{\partial k}{\partial x_j}\right] + G_k + G_b - \rho\varepsilon - Y_M + S_k \quad (3)$$

and,

$$\frac{\partial}{\partial t}(\rho\varepsilon) + \frac{\partial}{\partial x_j}(\rho\varepsilon u_j) = \frac{\partial}{\partial x_j}\left[\left(\mu + \frac{\mu_t}{\sigma_\varepsilon}\right)\frac{\partial \varepsilon}{\partial x_j}\right] + \rho C_1 S\varepsilon - \rho C_2 \frac{\varepsilon^2}{k+\sqrt{v\varepsilon}} + C_{1\varepsilon}\frac{\varepsilon}{k}C_{3\varepsilon}G_b + S_\varepsilon \quad (4)$$

The following base turbulence coefficients were set for this application: $C_1 = 1.44$, $C_2 = 1.92$ and $C_3 = 0.09$.

Energy equation

The conservation of energy equation used is as follows:

$$\frac{\partial}{\partial t}(\rho E) + \nabla.\left(\vec{v}\,(\rho E + p)\right) = \nabla.\left(k_{eff}\nabla T - \sum_j^n h_j \vec{J_j} + \left(\bar{\bar{\tau}}_{eff}.\vec{v}\right)\right) + S_h \quad (5)$$

For more details on the governing equations and formulation address to (Versteeg and Malalasekera, 1995; ANSYS, 2013).

Boundary conditions, the conditions set for the base CFD model configuration are presented in Table 3. Moreover, the conditions set for the optimized CFD model configuration are presented in Table 4. Modification of the boundary conditions in the optimized model was required due to the change in the multiphase model and mesh cell size.

The optimized model was assessed at the base case boundary conditions and no convergence was obtained. Depending on the mesh density and multiphase model defined, the courant number (if it is kept low) can converge as well as the CFD model. Therefore, it was necessary to modify the boundary conditions for the optimized case. Table 3 and Table 4 present the conditions identified for the convergence of the base case and optimized case simulation.

Regarding the methods applied for the resolution process, the solver type was pressure-based coupled with absolute velocity in transient flow. The formulation of absolute velocity was suggested for low flow velocities (ANSYS, 2013).

Similar to the boundary conditions modifications, the resolution method requires to be modified depending on the mesh cell number and multiphase model selected to facilitate the convergence of the CFD model. Table 5 shows the resolution methods established for the base case and optimized case.

Thermophysical properties of the single-phase fluids were obtained from the Fluent database. The water flow was set as incompressible whereas the properties of the materials were set constant. The thermodynamic properties such as density, viscosity, heat capacity, and thermal conductivity for the NH_3/$LiNO_3$ were obtained from (Libotean et al., 2007, 2008) and (Cuenca et al., 2014). The solution enthalpy was estimated as in (Haltenberger, 1939; McNeely, 1979).

Global Digital Central
ISSN: 2151-8629

Table 3 Boundary conditions for the base case.

Zone	*Boundary*	*Value*	*details*
Annulus side inlet	Inlet Pressure; direction specification method: normal to boundary	2.0×10^5 Pa	I = 0.185 %, k = 0.1006 $m^2.s^{-2}$; ε = 0.172 $m^2.s^{-3}$ velocity = 0.212 $m.s^{-1}$; volume fraction of phase 3 (water): 1.0
Inner tube inlet		5.16×10^5 Pa	I = 0.316 %; k = 2.53×10^{-3} $m^2.s^{-2}$; ε = 4.03×10^{-4} $m^2.s^{-3}$; velocity = 0.2076 $m.s^{-1}$; volume fraction of phase 4 (solution $NH_3/LiNO_3$): 0.452 XNH_3
Injector inlet		5.5×10^5 Pa	I = 0.567 %; k = 7.17×10^{-5} $m^2.s^{-2}$; ε = 1.07×10^{-6} $m^2.s^{-3}$; velocity = 1.78 $m.s^{-1}$; volume fraction of phase 2 (ammonia vapor): 1.0
Outer tube outlet	Outlet Pressure; direction specification method: normal to boundary		k = 0.01 $m^2.s^{-2}$; ε = 0.01 $m^2.s^{-3}$ Pressure = 2.0×10^5 Pa
Inner tube outlet			k = 0.01 $m^2.s^{-2}$; ε = 0.01 $m^2.s^{-3}$ Pressure = 5.13×10^5 Pa
Injector outlet	Contact region-interface		Pressure = 5.13×10^5 Pa
Walls	Stationary Wall		Steel

* Re: Reynolds number; I: turbulence intensity; k and ε: parameters of the turbulence model.

Table 4 Boundary conditions for the optimization case.

Zone	*Boundary*	*Value*	*Observations*
Annulus side inlet	Inlet Velocity	0.212084 $m.s^{-1}$	I = 0.185 %; k = 0.1006 $m^2.s^{-2}$; ε = 1.72 $m^2.s^{-3}$; volume fraction of phase 3 (water): 1.0
Inner tube inlet		0.2636 $m.s^{-1}$	I = 0.316 %; k = 2.53 $m^2.s^{-2}$; ε = 4.03 $m^2.s^{-3}$; volume fraction of phase 4 (solution $NH_3/LiNO_3$): 0.452 XNH_3
Injector inlet		1.78 $m.s^{-1}$	I = 0.567 %; k = 7.17×10^{-5} $m^2.s^{-2}$; ε = 1.07×10^{-6} $m^2.s^{-3}$; volume fraction of phase 2 (ammonia vapor): 1.0
Outer tube outlet	Outlet Pressure		k = 0.01 $m^2.s^{-2}$; ε = 0.01 $m^2.s^{-3}$
Inner tube outlet			k = 0.01 $m^2.s^{-2}$; ε = 0.01 $m^2.s^{-3}$
Injector outlet	Contact region-interface		Pressure = 5.13×10^5 Pa
Walls	Stationary Wall		Steel

* Re: Reynolds number; I: turbulence intensity; k and ε: parameters of the turbulence model.

Table 5 Solution methods established.

Variable	*CFD model base case*	*CFD model optimized*
	Methods	*Methods*
Scheme	PISO	Coupled
Momentum	Third-Order-MUSCL	
Pressure	Presto	
Gradient	Least squares cell-based	
Volume fraction	Compressive	QUICK
Transient formulation	Second-order implicit	
Energy	Third-Order-MUSCL	
Turbulent dissipation rate	Third -Order-MUSCL	
Turbulent kinetic energy	Third -Order-MUSCL	

Model validation procedure, the predicted results were contrasted with the experimental results depicted by Amaris (2013) for an $NH_3/LiNO_3$ tubular bubble absorber under the same operating conditions. The normality of the predicted and experimental results was assessed by applying the Shapiro Wilks test (n >50) and considering a P > 0.05 which indicates normality. The T-student test was employed to contrast the mean, the Mann-Whitney test was employed to contrast the ranges, whereas the Levene test was employed to contrast variances (n > 50). A value P > 0.05 suggests no statistically significant discrepancies between the results contrasted. Various accuracy tests were performed to contrast the selected parameters with the experimental results. The accuracy tests comprise the absolute mean deviation (AMD%), the relative mean deviation (RMD%), the sum of the squared errors (SSE), the root mean square error (RMSE), and root mean square deviation (RMSD).

3. RESULTS AND DISCUSSION

3.1 VOF and mixture models results

The literature shows that the CFD modelling of absorbers in VARS has been developed using two multiphase models: Volume of Fluid (VOF) (Asfand et al., 2015; Hosseinnia et al., 2016) and Mixture (Panda and Mani, 2016). Therefore, both multiphase models were used in both the base and optimized CFD models.

When assessing the base CFD model, the VOF model had a satisfactory performance. However, there was no converge to the solution using mesh 3 (i.e., 128877 elements). The VOF model is applied to fixed Eulerian meshes and it is suitable for immiscible fluids where the fluids interface plays a key role. For time-dependent calculations, it refines the time step for the integration of the volume fraction equation by modifying the Courant number under 250. This implies that the reduction of the time step to 1/1000 to 1/10000 or 1/100000 involves a significant increase in the Courant number, computational time and memory requirements, which leads to no converged solution. The VOF model has good performances in geometries with a low density of mesh elements, where the smallest time step is suitable. Therefore, when optimizing the mesh by increasing the number of mesh elements, which decreases the volume of the cell, it is recommended to change from the VOF multiphase model to the Mixture model for better modelling performance and convergence.

3.2 Mesh test results

The grid independence test applied to the base case using the solution temperature and concentration of ammonia at the outlet of the control volume is shown in Table 6. These variables were used following the recommendations by Lima et al. (2019).

Results show that predicted values using four meshes are not significantly different from the experimental solution temperature (320.95 K) and concentration (0.4587), at the absorber outlet. Table 6

Global Digital Central
ISSN: 2151-8629

shows that the calculated error of the chosen parameters with the four meshes considered is lower than 3.2 %. Therefore, the CFD model describes with good precision the variables selected for all meshes. However, the calculation time and memory requirements for mesh 1 are lower than meshes 2, 3 and, 4.

Mesh 2 computational time rose by 44% if compared to that of mesh 1. Results for mesh 3 show a deviation for the solution temperature around 50% lower than that for mesh 1, while the deviation for the concentration is 94% lower, however, the calculation time increased by 156%. Finally, the results for mesh 4 show a deviation for the solution temperature around 67% lower than that for mesh 1, while the deviation for the concentration is 48% lower. In this case, the calculation time increased up to 367%. Based on these results, it is observed that the calculation time increased linearly with the mesh density, while the deviation dropped at a lower rate.

Based on the values of error, calculation time, and memory requirements, it is concluded that mesh 1 is adequate to assess the absorber performance. The number of elements used in mesh 1 is similar to the number of elements used by Lima et al. (2019). However, the discussion in the next section shows that these outlet parameters cannot be recommended for an adequate validation of the CFD model. Therefore, additional verifications were needed in this case.

Table 6 Outlet temperature and ammonia concentration vs mesh elements.

Mesh	*Elements.*	*CFD results*		*Error (%)*		*Time (h)*	*Mem. use (Mb)*
		T_S (K)	Outlet X_{NH3} (w/w)	*T*	NH_3		
4	554804	319.6	0.466	0.4	1.6	8.4	1.2
3	128877	318.5	0.453	0.6	0.2	4.6	1.0
2	87326	317.6	0.472	1.0	2.8	2.6	0.5
1	27402	317.2	0.473	1.2	3.1	1.8	0.5

* Outlet solution temperature (TS), ammonia concentration (XNH_3), computational time (time), memory use (Mem. use).

3.3 Heat and mass transfer

This section shows the results from simulating the absorber performance using the CFD model. These results are contrasted with the experimental data reported by Amaris (2013). The experimental uncertainties reported were 5.7% and 13.4% for the absorbed mass flux and heat transfer coefficient of the solution side, respectively.

Table 7 presents the results from the base CFD model configuration for ammonia concentration and absorbed mass flux. The results show the base CFD model configuration calculated the ammonia concentration with errors lower than 0.7%, with a mean error of 0.47%, if contrasted to the experimental results, as was demonstrated with the mesh independence assessment. Furthermore, the results indicated that meshes with a small number of finite elements have satisfactory performance to predict the ammonia concentration at the absorber outlet. However, the absorbed mass flux predicted with the base CFD model shows errors between 9.5% and 42.9%, with a mean error of 24.7%. Since the absorption mass flux is frequently used for dimensioning absorbers, the base CFD model with a mesh of 27,402 elements is inadequate under the considered configuration. In that sense, a mesh refinement was required to improve the performance of the model by increasing the elements from 27,402 to 230,791 and modifying the boundary conditions and solution method.

Table 8 shows the results from the optimized CFD model configuration for ammonia concentration and absorbed mass flux.

Results show that, as compared to the experimental information, the optimized CFD model configuration predicted the ammonia concentration with errors lower than 1.4%, with a mean value of 0.36%.

Table 7 Results from experimental and base CFD model configuration for mass transfer parameters.

#	T_W (K)	$m_{in\text{-}W}$ (kg.s^{-1})	$m_{in\text{-}S}$ (kg.s^{-1})	*Exp*	*Cal*	*Error (%)*	*Exp*	*Cal*	*Error (%)*
				Outlet X_{NH3}			*Fab* $\times 10^{-3}$ (kg.m^{-2}s^{-1})		
1	313.8	102.0	20.3	0.459	0.460	0.3	3.2	3.6	9.5
2	313.8	101.5	30.2	0.455	0.457	0.4	3.4	4.1	16.4
3	313.8	105.2	40.4	0.453	0.455	0.5	3.4	4.3	22.1
4	313.8	106.9	50.3	0.453	0.455	0.2	3.4	4.5	24.0
5	314.0	105.8	60.2	0.453	0.456	0.7	3.5	5.9	39.9
6	313.9	109.5	71.5	0.450	0.453	0.5	3.3	5.7	42.9
7	308.7	105.4	30.0	0.455	0.458	0.6	3.9	5.2	25.4
8	308.8	91.3	40.6	0.455	0.458	0.7	3.9	5.1	22.4
9	308.8	90.6	49.7	0.454	0.456	0.5	4.0	6.0	32.6
10	308.6	105.6	64.8	0.451	0.453	0.4	4.2	5.6	26.2
11	308.7	91.1	20.5	0.459	0.461	0.4	3.9	4.4	11.1

* Water temperature (T_W), inlet water mass flow ($m_{in\text{-}W}$), inlet solution mass flow ($m_{in\text{-}S}$), ammonia concentration (X_{NH3}), NH_3 absorption mass flux (Fab), experimental (Exp), calculated (Cal).

Table 8 Results from experimental and optimized CFD model configuration for mass transfer parameters.

#	T_W (K)	$m_{in\text{-}W}$ (kg.s^{-1})	$m_{in\text{-}S}$ (kg.s^{-1})	*Exp*	*Cal*	*Error (%)*	*Exp*	*Cal*	*Error (%)*
				Outlet X_{NH3}			*Fab* $\times 10^{-3}$ (kg.m^{-2}s^{-1})		
1	313.8	102.0	20.3	0.459	0.453	1.4	3.2	3.2	1.7
2	313.8	101.5	30.2	0.455	0.453	0.6	3.4	3.4	0.8
3	313.8	105.2	40.4	0.453	0.453	0.1	3.3	3.2	3.0
4	313.8	106.9	50.3	0.453	0.453	0.1	3.4	3.2	6.1
5	314.0	105.8	60.2	0.453	0.453	0.1	3.5	3.3	6.6
6	313.9	109.5	71.5	0.451	0.453	0.5	3.3	4.2	-28
7	308.7	105.4	30.0	0.455	0.453	0.6	3.9	4.0	2.6
8	308.8	91.3	40.6	0.455	0.454	0.1	3.9	3.8	3.6
9	308.8	90.6	49.7	0.454	0.453	0.2	4.0	3.7	8.1
10	308.9	105.6	64.8	0.451	0.451	0.1	4.2	4.4	6.0
11	308.7	91.1	20.5	0.459	0.458	0.2	3.9	3.8	3.0

* Water temperature (T_W), inlet water mass flow ($m_{in\text{-}W}$), inlet solution mass flow ($m_{in\text{-}S}$), ammonia concentration (X_{NH3}), NH_3 absorption mass flux (Fab), experimental (Exp), calculated (Cal).

Moreover, the error for the absorption mass flux was lower than 28% with a mean error of 6.67%. Particularly, for experiment No. 6 (showing -28% of error for the absorption mass flux) there is no convergence to a solution, which is explained because of the biggest inlet flow solution considered for the model conditions defined in Table 4. In

Global Digital Central
ISSN: 2151-8629

this case, the solution method modifications and the mesh refinement method implemented by increasing mesh elements from 27402 to 230791, reduced the model error for the absorption mass flux from 24.7% to 6.67%.

Fig. 4 compares the results from the CFD model to the experimental data of the absorption mass flux. The data presented include the calculations for both, the base and optimized CFD model configurations.

The results from the base CFD model configuration show a low correspondence with the experimental results with no clear trend. Results from the optimized model configuration show a clear trend with a slope close to 45°. Overall, the slope from the results of the base CFD model configuration shows a sharper slope contrasted to the slope from the results of the optimized CFD model configuration. These results indicate that the optimized CFD model configuration can simulate the absorption mass flux for different solution mass flows and water temperatures (see Table 8). In general, table 8 shows that the absorbed mass flux increases as the mass flow of the solution increases and the temperature of the cooling water drops. Accordingly, the absorbed mass flux obtained from the CFD study ranged between 3.2×10^{-3} kg.m^{-2}.s^{-1} and 4.4×10^{-3} kg.m^{-2}.s^{-1}.

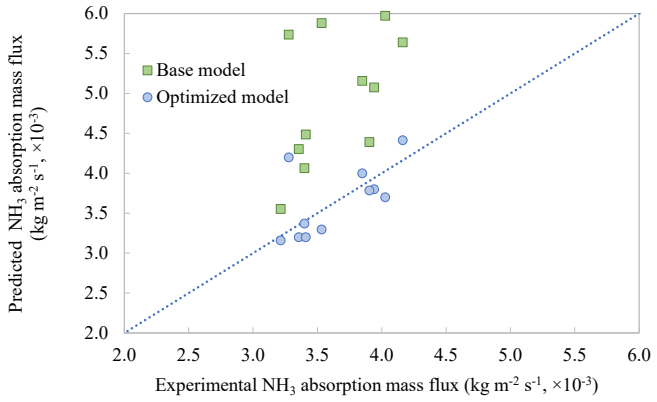

Fig. 4 Comparison of predicted and experimental results for the absorption mass flux.

Table 9 Experimental (Exp) and estimated (Cal) heat transfer parameters with the base CFD model configuration.

#	T_W (K)	$m_{in\text{-}W}$ (kg.s^{-1})	$m_{in\text{-}S}$ (kg.s^{-1})	T_S (K) Exp	T_S (K) Cal	Error (%)	h_S (W.m^{-2}K^{-1}) Exp	h_S (W.m^{-2}K^{-1}) Cal	Error (%)
1	313.8	102.0	20.3	320.9	318.1	0.9	509	664	23
2	313.8	101.5	30.2	321.0	318.2	0.9	552	660	16
3	313.8	105.2	40.4	321.2	319.4	0.6	641	660	3
4	313.8	106.9	50.3	321.3	320.1	0.4	734	661	10
5	314.0	105.8	60.2	321.5	319.9	0.5	671	662	1
6	313.9	109.5	71.5	321.3	320.4	0.3	689	662	4
7	308.7	105.4	30.0	318.7	317.1	0.5	641	663	3
8	308.8	91.3	40.6	319.2	317.5	0.5	698	663	5
9	308.8	90.6	49.7	319.2	317.7	0.5	733	763	4
10	308.6	105.6	64.8	319.7	318.1	0.5	807	663	18
11	308.7	91.1	20.5	318.9	317.6	0.4	481	551	13

Moreover, the error for the absorption mass flux was lower than 28% with a mean error of 6.67%. Particularly, for experiment No. 6 (showing -28% of error for the absorption mass flux) there is no convergence to a solution, which is explained because of the biggest inlet flow solution considered for the model conditions defined in Table 4. In this case, the solution method modifications and the mesh refinement method implemented by increasing mesh elements from 27402 to 230791, reduced the model error for the absorption mass flux from 24.7% to 6.67%.

Table 10 presents the temperature and heat transfer coefficient results for the solution flow, calculated with the optimized CFD model configuration, and those experimentally obtained.

Results show that for the optimized CFD model configuration, the outlet solution temperature is calculated with errors lower than 1.1%, with a mean error of 0.57%. moreover, the solution heat transfer coefficient is calculated with errors lower than 5.9%, with a mean error of 3.3%.

Table 10 Experimental (Exp) and estimated (Cal) heat transfer parameters with the optimized CFD model configuration.

#	T_W (K)	$m_{in\text{-}W}$ (kg.s^{-1})	$m_{in\text{-}S}$ (kg.s^{-1})	T_S (K) Exp	T_S (K) Cal	Error (%)	h_S (W.m^{-2}K^{-1}) Exp	h_S (W.m^{-2}K^{-1}) Cal	Error (%)
1	313.8	102.0	20.3	320.9	317.5	1.1	509	491	3.5
2	313.8	101.5	30.2	321.0	318.1	0.9	552	539	2.3
3	313.8	105.2	40.4	321.2	319.0	0.7	641	619	3.4
4	313.8	106.9	50.3	321.3	319.1	0.7	734	709	3.5
5	314.0	105.8	60.2	321.5	319.0	0.8	671	648	3.4
6	313.9	109.5	71.5	321.3	319.1	0.7	689	661	4.1
7	308.7	105.4	30.0	318.7	318.2	0.2	642	604	5.9
8	308.8	91.3	40.6	319.2	317.7	0.5	698	678	2.8
9	308.8	90.6	49.7	319.2	318.5	0.2	733	733	0.1
10	308.9	105.6	64.8	319.7	318.9	0.2	807	787	2.5
11	308.7	91.1	20.5	318.9	317.9	0.3	481	457	5.0

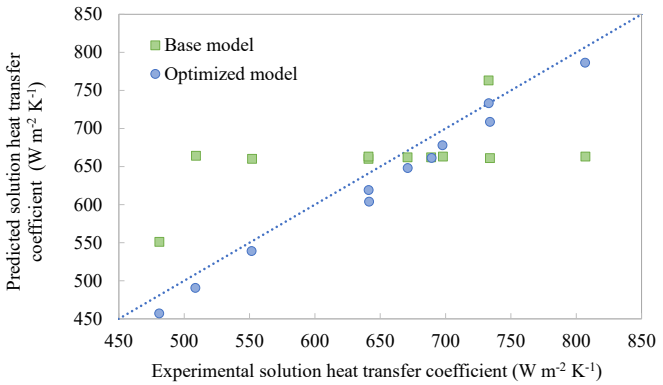

Fig. 5 Comparison of predicted and experimental results for the heat transfer coefficient.

Fig. 5 shows the calculated and experimental results for heat transfer coefficient. The calculated values include results from both, the base and optimized CFD model configurations. While the results show higher errors for the base CFD model configuration, these errors are low.

Moreover, the results for the optimized CFD model configuration show lower errors with a clear trend of the values, while the slope of the results is close to 45°. Overall, the results from the base CFD model configuration show no clear trend, with a slope lower than the results of the optimized CFD model configuration. Results indicate that the use of the optimized CFD model configuration is possible to accurately predict the solution heat transfer coefficient for different values of solution mass flow and cooling water temperature (see Table 10). In general, the heat transfer coefficient rises as the mass flow of the solution increases and the temperature of the cooling water drops. Since the heat transfer is linked to the mass transfer in absorbers, the higher the heat transfer, the better the mass transfer when the solution equilibrium conditions at the absorber outlet are still not reached. In this case, the heat transfer coefficient for the solution side ranged between 457 $W.m^{-2}.K^{-1}$ and 786 $W.m^{-2}.K^{-1}$.

3.4 Model Validation

The Shapiro-Wilks test shows that the ammonia concentration is the only variable with a normal distribution. Therefore, the T-student test was implemented to contrast the mean between the experimental and simulated data, while the Mann-Whitney test was implemented to contrast the ranges and the Levene test to contrast variances between the experimental data and simulated data obtained with the base and optimize CFD model. The statistical assessment for the base configuration model is shown in Table 8.

The results of the accuracy-test for the base CFD model configuration showed a satisfactory performance for the ammonia concentration and temperature variables with deviations between 1 % and 18 %. However, the absorbed mass flux and heat transfer coefficient showed larger deviations, between 1% and 132% indicating that the validation of the model must include the mass and heat transfer parameters because these are more sensitive variables and used for the absorber designing.

The statistical assessment for the optimized configuration model is shown in Table 9.

Table 8 Statistical assessment of the results from the base CFD model configuration, experimental (Exp) vs estimated (Cal).

Test	*Exp*	*Cal*	*Exp*	*Cal*
	Outlet X_{NH3} ($kg_{NH3}\cdot kg^{-1}_{NH3/LiNO3}$)		T_S (K)	
AMD%[1]	0.002	0.002	0.900	1.015
RMD%[2]	0.610	0.580	0.340	0.370
SSE[3]	0.0001	0.0001	11.6291	13.7273
RMSE[4]	0.00001	0	1.057	1.248
RMS[5]	0.4543	0.45653	320.0926	318.5565
Test	*Exp.*	*Cal.*	*Exp.*	*Cal.*
	Fab *(kg.m^{-2}s^{-1})*		h_S ($W.m^{-2}K^{-1}$)	
AMD%[1]	0.0003	0.0007	77.95	20.54
RMD%[2]	9.280	16.650	15.450	7.180
SSE[3]	0.0000	0.0000	101065	22640
RMSE[4]	0.0000	0.0000	9187.70	2058.18
RMS[5]	0.0037	0.004995	657.5691	662.6095

[1]Absolute mean deviation; [2]Relative mean deviation; [3]Sum of the squared errors; [4]Root mean square error; [5] Root mean square deviation
* Outlet solution temperature (T_S), ammonia concentration (X_{NH3}), NH_3 absorption mass flow (Fab), and solution heat transfer coefficient (h_S).

The results showed no statistical discrepancies between experimental, and model calculated results. The optimized model configuration implemented through a mesh refinement method reduced significantly the statistical deviations contrasted to the base model between a range of 1% and 11%. This indicates that the optimized CFD model configuration was adequate to simulate the heat and mass transfer processes in the absorber. In this case, it was not necessary to implement the use of user-defined functions (UDF) to vary the thermophysical properties of the fluid which means that the optimization method has a relevant weight on the CFD model performance. Based on the results in Table 8 and Table 9, it is concluded that the absorption mass flux and the heat transfer coefficient of the solution heat transfer coefficient are the variables recommended to validate a CFD model and simulate absorbers in VARS. Moreover, validation should be conducted using a series of experimental data to ensure an appropriate prediction of the absorption performance parameters at different operating conditions.

Table 9 Statistical assessment of the results from the optimized CFD model configuration, experimental (Exp) vs estimated (Cal).

Test	*Exp*	*Cal*	*Exp*	*Cal*
	Outlet X_{NH3} ($kg_{NH3}\cdot kg^{-1}_{NH3/LiNO3}$)		T_S (K)	
AMD	0.0020	0.0020	1.030	0.920
RMD	0.61000	0.50000	0.34000	0.29000
SSE	0.00006	0.00003	11.629	12.564
RMSE	0.00001	0.00000	1.05719	1.24000
RMSD	0.45430	0.45322	320.09256	318.44869
Test	*Exp.*	*Cal.*	*Exp.*	*Cal.*
	Fab ($kg.m^{-2}s^{-1}$)		h_S ($W.m^{-2}K^{-1}$)	
AMD	0.0003	0.0003	78.0.	79.60
RMD	9.28000	11.95000	15.45000	16.13000
SSE	0.00000	0.00000	101065	103100
RMSE	0.00000	0.00000	9188	9373
RMSD	0.00366	0.00367	658	634

* Outlet solution temperature (T_S), ammonia concentration (X_{NH3}), NH_3 absorption mass flow (Fab), solution heat transfer coefficient (h_S).

4. CONCLUSIONS

In this paper, the optimization of a CFD model to predict the heat and mass transfer performance of a bubble absorber using the $NH_3/LiNO_3$ mixture is presented. The methodology to build up the model and its validation are detailed in this case. The main conclusions from the present study can be drawn as follows

- The absorbed mass flux and heat transfer coefficient of the solution side are parameters that must be considered in the validation process of CFD models for absorbers because these are more sensitive variables for the CFD absorber performance. Moreover, the validation process should be conducted with data from a set of experimental tests, rather than just considering the results from one experimental test.
- Implementing the optimization conditions defined for the CFD model results in avoiding any significant statistical difference between experimental and calculated results values for the variables considered. While the CFD model using the VOF model converged at a low density of mesh elements, the Mixture model was required for the convergence of the CFD model at a high density of mesh elements.

- The optimized CFD model was found suitable to simulate the performance of the tubular bubble absorber as solution flow and heat dissipation temperature varied. The absorption mass flux was up to 4.4×10^{-3} kg $m^{-2}s^{-1}$, while the solution heat transfer coefficient was up to 786 W $m^{-2}K^{-1}$ for the conditions considered.
- The methodology details the development of a CFD model to simulate an absorber in VARs and can be applied to develop an improved bubble absorber arrangement and explore the absorber performance with new working fluids. Further studies can include the assessment of different absorber configurations considering internal details such as flow patterns and local heat and mass transfer parameters.

REFERENCES

Aggarwal, M. K., and Agarwal, R. S. (1986). Thermodynamic properties of lithium nitrate-ammonia mixtures. *Int. J. Energy Res.* 10, 59–68. https://doi.org/10.1002/er.4440100107

Amaris, C. (2013). Intensification of NH3 bubble absorption process using advanced surfaces and carbon nanotubes for NH3/LiNO3 absorption chillers. Available at: https://www.tdx.cat/handle/10803/128504

Amaris, C., Alvarez, M. E., Vallès, M., and Bourouis, M. (2020a). Performance assessment of an NH3/LiNO3 bubble plate absorber applying a semi-empirical model and artificial neural networks. *Energies* 13. https://doi.org/10.3390/en13174313

Amaris, C., and Bourouis, M. (2021). Boiling process assessment for absorption heat pumps: A review. *Int. J. Heat Mass Transf.* 179, 121723. https://doi.org/10.1016/j.ijheatmasstransfer.2021.121723

Amaris, C., Bourouis, M., Vallès, M., Salavera, D., and Coronas, A. (2015). Thermophysical properties and heat and mass transfer of new working fluids in plate heat exchangers for absorption refrigeration systems. *Heat Transf. Eng.* 36. https://doi.org/10.1080/01457632.2014.923983

Amaris, C., Miranda, B. C., and Balbis-Morejón, M. (2020b). Experimental thermal performance and modelling of a waste heat recovery unit in an energy cogeneration system. *Therm. Sci. Eng. Prog.* 20. https://doi.org/10.1016/j.tsep.2020.100684

Amaris, C., Rodriguez, A., Sagastume, A., and Bourouis, M. (2023). Performance Assessment of a Solar/Gas Driven NH3/LiNO3 Absorption Cooling System for Malls. *Lect. Notes Mech. Eng.*, 311–328. https://doi.org/10.1007/978-981-19-3467-4_19

Amaris, C., Vallès, M., and Bourouis, M. (2018). Vapour absorption enhancement using passive techniques for absorption cooling/heating technologies: A review. *Appl. Energy* 231, 826–853. https://doi.org/10.1016/j.apenergy.2018.09.071

Anand, S., Suresh, S., Dhanuskodi, R., and Santhosh Kumar, D. (2020). Comparison of cfd and empirical models for predicting wall temperature at supercritical conditions of water. *Front. Heat Mass Transf.* 14. https://doi.org/10.5098/hmt.14.8

ANSYS (2013). *ANSYS Fluent Theory Guide*. , ed. Ansys New York, USA https://doi.org/10.1016/0140-3664(87)90311-2

Asfand, F., Stiriba, Y., and Bourouis, M. (2015). CFD simulation to investigate heat and mass transfer processes in a membrane-based absorber for water-LiBr absorption cooling systems. *Energy*. https://doi.org/10.1016/j.energy.2015.08.018

Asfand, F., Stiriba, Y., and Bourouis, M. (2016). Performance evaluation of membrane-based absorbers employing H2O/(LiBr + LiI + LiNO3 + LiCl) and H2O/(LiNO3 + KNO3 + NaNO3) as working pairs in absorption cooling systems. *Energy*. https://doi.org/10.1016/j.energy.2016.08.103

Ayou, D. S., Bruno, J. C., Saravanan, R., and Coronas, A. (2013). An overview of combined absorption power and cooling cycles. *Renew. Sustain. Energy Rev.* 21, 728–748. https://doi.org/10.1016/j.rser.2012.12.068

Bhagat, R. D., and Deshmukh, S. J. (2022). Numerical analysis to predict the behavior of liquid vapor slug flow in vertically placed u-shaped closed capillary tube. *Front. Heat Mass Transf.* 19. https://doi.org/10.5098/hmt.19.14

Cerezo, J. (2006). Estudio del proceso de absorción con amoníaco-agua en intercambiadores de placas para equipos de refrigeración por absorción.

Cuenca, Y., Salavera, D., Vernet, A., Teja, A. S., and Vallès, M. (2014). Thermal conductivity of ammonia + lithium nitrate and ammonia + lithium nitrate + water solutions over a wide range of concentrations and temperatures. *Int. J. Refrig.* 38, 333–340. https://doi.org/10.1016/j.ijrefrig.2013.08.010

Elperin, T., and Fominykh, A. (2003). Four stages of the simultaneous mass and heat transfer during bubble formation and rise in a bubbly absorber. *Chem. Eng. Sci.* 58, 3555–3564. https://doi.org/10.1016/S0009-2509(03)00192-1

Florides, G. A., Tassou, S. A., Kalogirou, S. A., and Wrobel, L. C. (2002). Review of solar and low energy cooling technologies for buildings. *Renew. Sustain. Energy Rev.* 6, 557–572. https://doi.org/10.1016/S1364-0321(02)00016-3

Haltenberger, W. (1939). Enthalpy-Concentration Charts from Vapor Pressure Data. *Ind. Eng. Chem.* 31, 783–786. https://doi.org/10.1021/ie50354a032

Hosseinnia, S. M., Naghashzadegan, M., and Kouhikamali, R. (2016). CFD simulation of adiabatic water vapor absorption in large drops of water-LiBr solution. *Appl. Therm. Eng.* 102, 17–29. https://doi.org/10.1016/j.applthermaleng.2016.03.144

Hosseinnia, S. M., Naghashzadegan, M., and Kouhikamali, R. (2017). CFD simulation of water vapor absorption in laminar falling film solution of water-LiBr ─ Drop and jet modes. *Appl. Therm. Eng.* 115, 860–873. https://doi.org/10.1016/j.applthermaleng.2017.01.022

Kang, Y. T., Akisawa, A., and Kashiwagi, T. (2000). Analytical investigation of two different absorption modes: falling film and bubble types. *Int. J. Refrig.* 23, 430–443. https://doi.org/10.1016/S0140-7007(99)00075-4

Kang, Y. T., Kashiwagi, T., and Christensen, R. N. (1998). Ammonia-water bubble absorber with a plate heat exchanger. in *ASHRAE Transactions*, 1565–1575.

Karima, A., Djamel, S., Ali, N., and Houari, A. (2018). CFD investigations of thermal and dynamic behaviors in a tubular heat exchanger with butterfly baffles. *Front. Heat Mass Transf.* 10. https://doi.org/10.5098/hmt.10.27

Libotean, S., Martín, A., Salavera, D., Valles, M., Esteve, X., and Coronas, A. (2008). Densities, viscosities, and heat capacities of ammonia + lithium nitrate and ammonia + lithium nitrate + water solutions between (293.15 and 353.15) K. *J. Chem. Eng. Data* 53, 2383–2388. https://doi.org/10.1021/je8003035

Libotean, S., Salavera, D., Valles, M., Esteve, X., and Coronas, A. (2007). Vapor-liquid equilibrium of ammonia + lithium nitrate + water and ammonia + lithium nitrate solutions from (293.15 to 353.15) K. *J. Chem. Eng. Data* 52, 1050–1055. https://doi.org/10.1021/je7000045

Lima, A. A. S., Ochoa, A. A. V, Da Costa, J. A. P., and Henríquez, J. R. (2019). CFD simulation of heat and mass transfer in an absorber that uses the pair ammonia/water as a working fluid. *Int. J. Refrig.* 98, 514–525. https://doi.org/10.1016/j.ijrefrig.2018.11.010

McNeely, L. A. (1979). Thermodynamic properties of aqueous solutions of lithium bromide. *ASHRAE Trans.* 85, 413–434.

Mendoza, J., Rhenals, J., Avila, A., Martinez, A., De la Vega, T., and Durango, E. (2021). Heat absorption cooling with renewable energies: a case study with photovoltaic solar energy and biogas in Cordoba, Colombia. *INGE CUC* 17, 1–10. https://doi.org/10.17981/ingecuc.17.2.2021.01

Merrill, T. L., and Perez-Blanco, H. (1997). Combined heat and mass transfer during bubble absorption in binary solutions. *Int. J. Heat Mass Transf.* 40, 589–603. https://doi.org/10.1016/0017-9310(96)00118-4

Mirzaie, M., Talebizadeh, A. R., and Hashemipour, H. (2020). CFD simulation of benzene adsorption on pistachio activated carbon porous media. *Front. Heat Mass Transf.* 14, 1–7. https://doi.org/10.5098/hmt.14.19

Oronel, C., Amaris, C., Vallès, M., and Bourouis, M. (2010). Experiments on the characteristics of saturated boiling heat transfer in a plate heat exchanger for ammonia/lithium nitrate and ammonia/(lithium nitratewater). in *2010 3rd International Conference on Thermal Issues in Emerging Technologies, Theory and Applications - Proceedings, ThETA3 2010*, 217–225. https://doi.org/10.1109/THETA.2010.5766401

Panda, S. K., and Mani, A. (2016). CFD heat and mass transfer studies in a R134a-DMF bubble absorber with swirl flow entry of R134a vapour. *Int. Compress. Eng. Refrig. Air Cond. High Perform. Build. Conf.*, 1–10.

Rodríguez-Toscano, A., Amaris, C., Sagastume-Gutiérrez, A., and Bourouis, M. (2022). Technical, environmental, and economic evaluation of a solar/gas driven absorption chiller for shopping malls in the Caribbean region of Colombia. *Case Stud. Therm. Eng.* 30, 101743. https://doi.org/10.1016/J.CSITE.2021.101743

Soheel, A. H., Jumaah, O. M., and Saleem, A. M. (2021). Simulation and investigation of nano-refrigerant fluid characteristics with the two-phase flow in microchannel. *Front. Heat Mass Transf.* 17. https://doi.org/10.5098/hmt.17.21

Suresh, M., and Mani, A. (2010). Heat and mass transfer studies on R134a bubble absorber in R134a/DMF solution based on phenomenological theory. *Int. J. Heat Mass Transf.* 53, 2813–2825. https://doi.org/10.1016/j.ijheatmasstransfer.2010.02.016

Triché, D., Bonnot, S., Perier-Muzet, M., Boudéhenn, F., Demasles, H., and Caney, N. (2017). Experimental and numerical study of a falling film absorber in an ammonia-water absorption chiller. *Int. J. Heat Mass Transf.* 111, 374–385. https://doi.org/10.1016/j.ijheatmasstransfer.2017.04.008

Turkyilmazoglu, M. (2019). Cooling of Particulate Solids and Fluid in a Moving Bed Heat Exchanger. *J. Heat Transfer* 141, 114501. https://doi.org/10.1115/1.4044590

Turkyilmazoglu, M. (2021). Heat absorption due to falling film with imposed uniform mass fraction at the wall. *Int. J. Heat Mass Transf.* 177, 121585. https://doi.org/10.1016/j.ijheatmasstransfer.2021.121585

Ullah, K. R., Saidur, R., Ping, H. W., Akikur, R. K., and Shuvo, N. H. (2013). A review of solar thermal refrigeration and cooling methods. *Renew. Sustain. Energy Rev.* 24, 499–513. https://doi.org/10.1016/j.rser.2013.03.024

Versteeg, H. K., and Malalasekera, W. (1995). *An introduction to computational fluid dynamics. The finite volume method*. 1st ed. , ed. Longman Group Ltd New York.

Wu, X., Xu, S., and Jiang, M. (2018). Development of bubble absorption refrigeration technology: A review. *Renew. Sustain. Energy Rev.* 82, 3468–3482. https://doi.org/10.1016/J.RSER.2017.10.109

Zapata, A., Amaris, C., Sagastume, A., and Rodríguez, A. (2021). CFD modelling of the ammonia vapour absorption in a tubular bubble absorber with NH3/LiNO3. *Case Stud. Therm. Eng.* 27, 101311. https://doi.org/10.1016/J.CSITE.2021.101311

Zhou, R., Wang, M., Jin, Z., and Li, S. (2023). Modeling and experimental verification of the enhancement of TiO2 nanofluid on ammonia falling film absorption process. *Int. J. Therm. Sci.* 184, 107917. https://doi.org/10.1016/j.ijthermalsci.2022.107917